Impedance-Based Force Transduction Within Fluid-Filled Parylene Microstructures

Christian A. Gutierrez, *Member, IEEE*, and Ellis Meng, *Senior Member, IEEE*

***Abstract*—We report on the use of electrochemical impedance (EI) as the basis for force transduction in Parylene-based microdevices. Electrolyte-filled microstructures were realized for extremely sensitive contact-force detection (10 mN range, ±0.023 mN resolution) enabled by EI-based transduction and are a promising platform for next-generation biomedical sensing technology. The design, fabrication, and characterization of Parylene-based electrochemical-MEMS (EC-MEMS) devices capable of microNewton contact-mode force measurement are presented and discussed. [2011-0040]**

***Index Terms*—Biomimetic, contact sensor, electrochemical-MEMS (EC-MEMS), electrochemical sensing, electrochemical transduction, force sensor, impedance-based sensor, liquid encapsulation, liquid impedance, mechanotransduction, Parylene C.**

I. Introduction

PARYLENE has gained popularity as a polymer material across various fields of research due to its versatility, conformal room temperature deposition, favorable mechanical and electrical properties, and biocompatibility (USP Class VI). The ability to micromachine Parylene has led to its use in sensors [1]–[4], actuators [5], [6], and various microfluidic components and systems [7]–[10]. This combination of attributes makes Parylene attractive for many biomedical applications. In this paper, we demonstrate the use of fluid-filled Parylene microstructures for highly sensitive force measurement intended for biomedical applications.

A variety of biomedical force sensing technologies exist [11]–[13]; however, oftentimes the underlying operating mechanisms (capacitive, electrostatic, piezoresistive, optical), developed for nonbiological applications, remain the same [14], [15]. As a result, these techniques can be difficult to implement in practical applications where they could be most beneficial. Biomedical force measurement is of particular interest to areas such as tactile feedback for minimally invasive surgery [12], tissue health diagnostics [16]–[18], surgical tool instrumentation [19], and real-time monitoring of acute applied pressures during delicate surgical procedures in the eye [20]–[22] or brain [23], [24] (e.g., retinal or cortical implant procedures). The use of elastomeric materials functionalized with conductive particles is a common approach; however, these technologies often lack the force sensitivity required for the most sensitive applications (0.01–1 mN), and are geared toward general surgical gripping and grasping requiring force sensitivity in the range of 0.1–11 N [25]. Traditional silicon-based techniques (cantilevers, diaphragms, combs) often require additional encapsulation techniques to protect the sensors from wet environments, and the requisite packaging can often prohibit practical implementation [26]. Furthermore, protective elastic coatings reduce sensitivity and function as low-pass spatial and temporal filters [27].

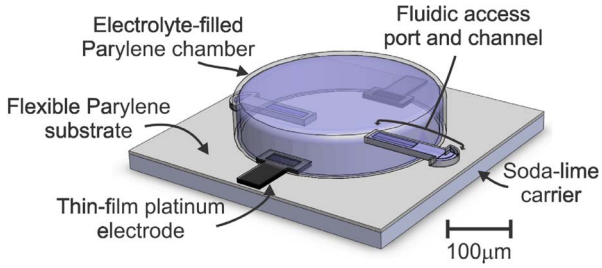

Fig. 1. Model of single sensor unit. A compliant electrolyte-filled Parylene microchamber enables EI-based force measurement. The sensor is fluidically coupled and open to the external environment through the fluidic access ports and channels.

To address these challenges, we previously demonstrated the use of Parylene as a substrate to fabricate flexible, electrolyte-filled microstructures for sensing and actuating applications [28], [29]. The use of Parylene brings improved mechanical coupling over traditional materials for applications involving intimate contact with biological tissues. The combination of microfluidics, electrochemistry, and mechanics form the basis of electrochemical-MEMS (EC-MEMS) technologies that present a promising platform for next-generation biomedical sensors. Here, we report on the development of a Parylene-based EC-MEMS sensor capable of microNewton contact-mode force transduction.

II. Device Design and Operation

The core of the device consists of a circular microchamber structure filled with a conductive aqueous electrolyte and a pair of microfabricated thin-film electrodes in contact with the electrolyte solution (Fig. 1). Additional microfluidic channels at the base of the chamber provide a pathway for fluidic coupling between the microchamber interior and the external environment. A pair of electrodes is located opposite one another on the interior perimeter of the chamber to maximize the path length over which electrochemical impedance (EI) measurements are taken. A circular diaphragm design was selected here

Manuscript received February 14, 2011; revised May 27, 2011; accepted June 19, 2011. Date of publication July 29, 2011; date of current version September 30, 2011. This work was supported in part by the Biomimetic Microelectronic Systems Engineering Research Center of the NSF, an NSF CAREER Award, and by the Bill and Melinda Gates Foundation (CG). Subject Editor C. Liu.

The authors are with the University of Southern California, Los Angeles, CA 90089 USA (e-mail: cagutier@usc.edu; ellis.meng@usc.edu).

Color versions of one or more of the figures in this paper are available online at http://ieeexplore.ieee.org.

Digital Object Identifier 10.1109/JMEMS.2011.2160935

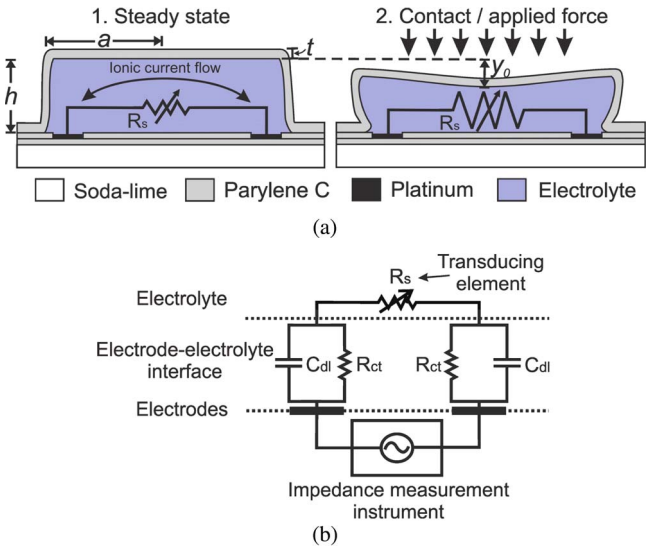

Fig. 2. (a) Electrochemical impedance transduction principle. (b) The electrical equivalent circuit model of the electrode–electrolyte interface.

for simplicity, however, additional sensor geometries are easily realized given that the impedance sensing technique can be applied between any electrode-pair arrangement provided that a fluid path exists. The use of Parylene C and thin-film platinum in the device construction enables the fabrication of flexible films with excellent biocompatibility. The sensors are ready to use after fabrication and, except for electrical connections, no additional materials or packaging processes are required at the sensor's mechanical interface.

The device is fluidically coupled to the external environment and therefore requires immersion in an aqueous medium for operation. This requirement, is however, compatible with the wet conditions usually encountered when working with soft tissues. Filling is accomplished by immersion in the operating environment, allowing the surrounding fluid to fill the chamber and function as the working electrolyte. The application of external forces on the chamber surface deforms the compliant fluid-filled structure and redistributes the enclosed fluid [Fig. 2(a)]. Variations in the volumetric conductive path of current-carrying ions in the fluid register as a change in the measured EI. In this manner, volumetric variations of an encapsulated electrolyte can be correlated to mechanical contact forces exerted by external sources on the sensor. The resulting impedance changes contain information about the magnitude of the externally applied force.

A. Electrochemical Considerations

The electrical equivalent circuit of the two-electrode system, depicted in Fig. 2(b), is based on the simplified Randles model where the parallel combination of the double layer capacitance (C_{dl}) and charge transfer resistance (R_{ct}) describes phenomenon at each electrode interface. Many electrochemical sensing applications employ potentiometric and amperometric detection techniques where changes to the electrode surface properties (due to binding and adsorption of species in the solution) are used as the basis for detection. Here, however, we apply a conductometric technique where characteristics of the solution (namely solution resistance) are leveraged for transduction, and interfacial phenomena occurring at the electrode surface are less important. Details regarding the electrochemical interface and associated surface phenomena have been well studied and can be found throughout the electrochemistry literature [30]–[34]; only a brief treatment relevant to the application presented here is provided.

EI is measured through application of a small alternating current (or voltage) across the thin-film electrodes and tracking the corresponding voltage (or current). These measurements can be performed with very little power ($< 100\ \mu$W) and produce only reversible electrochemical species. Consequently, hydrolysis of the electrolyte does not occur so long as the magnitude of the applied AC signal is maintained within the "water-window" of the electrode material ($\sim 1.4\ V_{pp}$ for platinum) where current is generated though reversible faradaic reactions. At sufficiently high frequencies, typically > 1 kHz, the contribution of the interfacial components (C_{dl} and R_{ct}) to the overall impedance is minimized as the capacitive reactance of C_{dl} becomes small (1). A limitation to this assumption often arises in the use of microelectrodes where electrode surface areas can be very small, thus increasing the reactance of C_{dl} appreciably. This is typically a concern for sharp point-tip electrodes where noise and attenuation can significantly impact measurement of small signals

$$Z(w) = R_s + \frac{2R_{ct}}{1 + jwR_{ct}C_{dl}}. \tag{1}$$

The value of C_{dl} per unit area for bright platinum at 1 kHz has been measured to be about 20 pF/cm^2[35]. The exposed area of each platinum electrode used here is $55 \times 25\ \mu$m ($1375\ \mu$m^2) yielding a capacitance of 275 pF at 1 kHz. The values of both R_{ct} and C_{dl} are in fact not constant as suggested by the model, but have been empirically found to vary with frequency scaling as $1/f^{0.5}$ [36]. Thus, by appropriate scaling, the capacitance value becomes 123 pF at 5 kHz and yields a capacitive reactance of 260 kΩ which is in line with values reported in the literature. Electrode impedances up to 5 MΩ are not uncommon and have been utilized extensively in single-unit neuronal signal recording. For instances in which the electrode impedance becomes significantly larger, for example with very small tip electrodes, platinization of the electrode surface through electrodeposition has proved effective in dramatically increasing surface area. An effective increase of 30–40 times over smooth platinum has been reported [20], [37], [38]. The charge transfer resistance, a parameter often difficult to measure experimentally, captures the resistance to changes in the equilibrium current within the double layer when an external potential is applied. It is generally considered to be the difference between the electrode impedance at very low frequency (< 0.1 Hz) and the solution resistance and is typically very high (10–100 MΩ). This assumption was verified by a parametric fit of the EI spectrum of several thin-film electrodes using standard electrochemical analysis software (Gamry Instruments, Echem Analyst) yielding R_{ct} values in excess of 30 MΩ. At the frequency utilized here (5 kHz), R_{ct} does not make

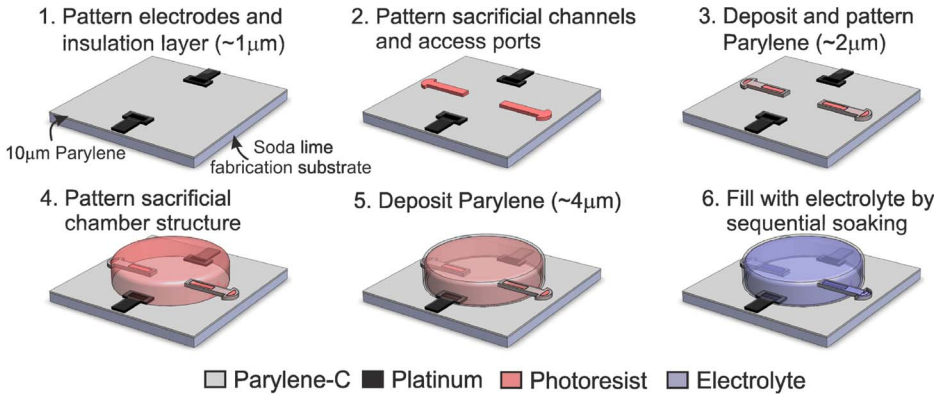

Fig. 3. Multilayered Parylene-based fabrication process performed at low temperature (90 °C).

an important contribution to the overall electrode impedance (relative to the capacitive reactance of C_{dl}).

It should also be noted that the exact values of C_{dl} and R_{ct} are of secondary importance given the use of a single measurement frequency at which these parameters can be considered constant. Conductometric variations (eg. solution resistance) are therefore the main source of changes to the measured impedance. The use of a low conductivity electrolyte, such as deionized (DI) water (< 10 μS/cm), further ensures that the solution resistance is the dominant parameter in the measured impedance value. Consequently, the impedance response can be approximately modeled as a simple classical resistance R_S, where ρ is the resistivity of the electrolyte, l is the distance between the electrodes, and A is the cross-sectional area of the fluid between the electrodes (2). The impedance is, therefore, inversely proportional to the cross-sectional area between the electrodes and is directly analogous to a variable "fluidic" resistor. This phenomenon enables the transduction and measurement of physical stimuli acting on the electrolyte-filled chamber

$$\Delta|Z|_{f>1\text{ khz}} \approx \Delta R_S = \frac{\rho l}{\Delta A}. \tag{2}$$

The length scale over which such an approximation is valid is determined by the characteristic Debye length which accounts for surface interactions occurring at the electrode surface. These include adsorbed ions on the metal surface which form the Helmholtz double layer and nonspecifically adsorbed ions in the adjacent diffuse layer. This length is also dependent on the concentration of solvated ions and decreases with increasing ionic strength. For a typical salt solution (eg. saline), this distance is $<$ 10 nm but can range up to $\sim$950 nm in the case of pure water [34], [39]. Beyond this region exists the bulk solution (i.e., homogenous charge distribution) and extends until a second electrode is encountered. For a two-electrode system in which the bulk solution resistance serves as the core transduction mechanism, the minimum electrode separation distance over which (2) is valid is estimated to be on the order $\sim$2 μm for low conductivity electrolytes and $\sim$20 nm for a high conductivity electrolyte. An electrode separation of $\sim$175 μm, utilized here, provides sufficient bulk solution to satisfy this assumption under a variety of working electrolytes.

B. Device Mechanics

Due to the circular chamber geometry, the force–deflection response most closely follows that of a pressure-loaded circular diaphragm with fixed edges. Although these boundary conditions are not strictly met due to slight deformation of the chamber sidewalls, the analytical results of this model sufficiently describe the sensor response. By adjusting parameters such as membrane thickness t, diaphragm radius a, and height h, the force–deflection performance can be easily tuned for a particular range (3) [40]:

$$P = \frac{16}{3(1-u^2)}\frac{Et^3}{a^4}y_0 + \frac{7-u}{3(1-u)}\frac{Et}{a^4}y_0^3 \tag{3}$$

where y_0 is center deflection, u is Poisson's ratio, E is modulus of elasticity, and P is pressure (assumed to be uniformly applied force distributed over surface area). Adjusting the sensor height will set the maximum deflection range of the sensors and impose an upper limit to the applied forces before the membrane touches down onto the substrate below. As will be discussed later, the effect of the integrated fluidic channels and ports only becomes significant if they are occluded or blocked. The most significant factor to the mechanical behavior is the viscous damping imposed by the surrounding solution which limits operation to low frequency ($<$ 200 Hz).

III. Device Fabrication

The entire fabrication process was realized at relatively low temperatures (90 °C) which enables its use on a variety of polymer substrates and facilitates adoption in temperature-sensitive processes (Fig. 3). Standard surface micromachining techniques were employed on a standard soda lime substrate (500 μm thick). First, Parylene was deposited (10 μm) on a wafer optionally treated with A-174 adhesion promoter (Specialty Coating Systems, Inc., Indianapolis, ID). The adhesion promoter facilitated handling of test devices which were diced into 1 cm^2 dies for characterization purposes and ensured adhesion to the substrate. Platinum electrodes (2000 Å) were deposited in an electron beam evaporator and patterned by lift-off using an image reversal photoresist with a negative sidewall profile (1.5 μm, AZ 5214-E, AZ Electronic Materials, Branchburg, NJ). Next, a Parylene insulation layer (1 μm)

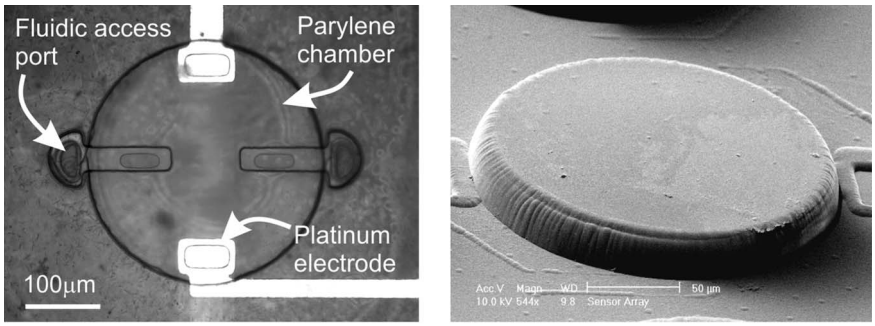

Fig. 4. (a) Optical micrograph of single device [41] and (b) scanning electron micrograph of device structure ([10] © IEEE 2010).

was deposited. Insulation over the electrodes was removed by reactive ion etching in oxygen plasma (100 W, 100 mT) utilizing a photoresist mask (4 μm, AZ 4400, AZ Electronic Materials, Branchburg, NJ). Photoresist (2–4 μm, AZ 4400, AZ Electronic Materials, Branchburg, NJ) was then spun-on and patterned forming a sacrificial mold for the fluidic access ports. This was followed by Parylene deposition (2 μm) and selective etching of Parylene over the fluidic port openings and electrode sites.

Removal of the photoresist etch mask proved to be difficult at this point due to the exposed fluidic port openings and resulted in erosion of the underlying sacrificial structures. Directly spinning an additional layer of photoresist on top of the existing etch mask at a calibrated speed enabled successful patterning of a second sacrificial photoresist layer (AZ 4620, AZ Electronic Materials, Branchburg, NJ) to form the microchamber mold (18–21 μm height, 200 μm diameter). A thorough softbake of this layer was essential to avoid solvent degassing and to minimize rounding of chamber features during the following steps. A final layer of Parylene (4.2 μm) was then deposited comprising the membrane and sidewalls of the chamber structure. The Parylene was etched using a 10–12 μm thick etch mask (AZ 4620, AZ Electronic Materials, Branchburg, NJ) to re-open the fluidic access ports on the exterior of the chamber exposing the underlying photoresist allowing for access and removal by immersion in baths of acetone and isopropyl alcohol. Due to the nonplanar structures during this final etch step, a thicker mask was necessary to prevent mask erosion and unwanted etching of the top edges of the chamber. Following a 24 h soak in the solvent baths, the devices were transferred to a DI water bath for rinsing ($\sim$6 h) and finally placed in a bath containing the desired electrolyte solution. Removal of sacrificial materials, rinsing, and filling occurred simultaneously across multiple devices in a wafer-level batch process. The Parylene film was optionally released from an untreated soda lime substrate by cutting with a razor blade, a process which was facilitated by immersion in water.

Fig. 4(a) is an optical micrograph of a device following removal of the sacrificial photoresist and filling with DI water. Fig. 4(b) is a scanning electron micrograph of a device prior to removal of any sacrificial materials showing the chamber protruding from the surface of the Parylene film. A thin layer of gold has been evaporated over the samples for scanning electron microscopy to avoid excess charging of the Parylene film.

IV. Experimental Methods

Test dies containing several devices were diced from a soda lime wafer substrate and mounted on a custom printed circuit board (PCB) with a cyanomethacrylate adhesive. Electrical connectivity to PCB-mounted dies was established by wire-bonding prior to removal of the sacrificial photoresist contained within the devices. A water-proof marine epoxy was then applied underwater and served two purposes: 1) insulation of the wirebond connections and 2) formation of a well to contain electrolyte such that devices were submerged during testing. Insulating the wirebonds was critical to avoid shorting of leads when the well was filled with electrolyte. This step was performed underwater to prevent devices from drying and collapsing due to stiction when exposed to air. Outside the well, electrical connections were soldered to contact pads and were kept dry during testing. The PCB-mounted devices were maintained in DI water for 24 h to allow full curing of the epoxy well. Although the ionic content of DI water is low, it is still capable of functioning as an electrolyte with a solution resistance typically in the 0.5–2 MΩ range. Various other solutions could function as an electrolyte, for example, human blood, body fluids, and cell culture media are all compatible with EI measurements [42].

Experiments were conducted on a floating optical table and controlled via a custom LabVIEW interface (National Instruments, Austin, TX) providing both control and measurement capability. PCBs were mounted onto an X-Y positioning stage secured to the optical table. Force measurements were acquired with a 50 g load cell (LCFA-50, Omega Engineering, Stamford, CT) mounted to a computer-controlled micropositioning stage providing accurate z-axis positioning capability (Z812, Thorlabs, Newton, NJ) (Fig. 5). This enabled real-time contact-mode force measurement during application of user-defined deflection profiles. EI measurements were acquired (5 kHz, 1 V_{pp}) concurrently by a precision LCR meter (E4980A, Agilent Inc, Santa Clara, CA) and logged by LabVIEW software.

A flat, polished probe tip measuring 500 μm in diameter was attached vertically in line with the load cell. The probe tip provided a defined contact surface large enough to deflect the entire sensor surface Fig. 6(a). Alignment of the tip was performed visually through an optical microscope attached to a goose-neck CCD capture device for flexibility. Contact between the probe tip and sensor was verified by concurrent increases in the measured force and impedance prior to application of

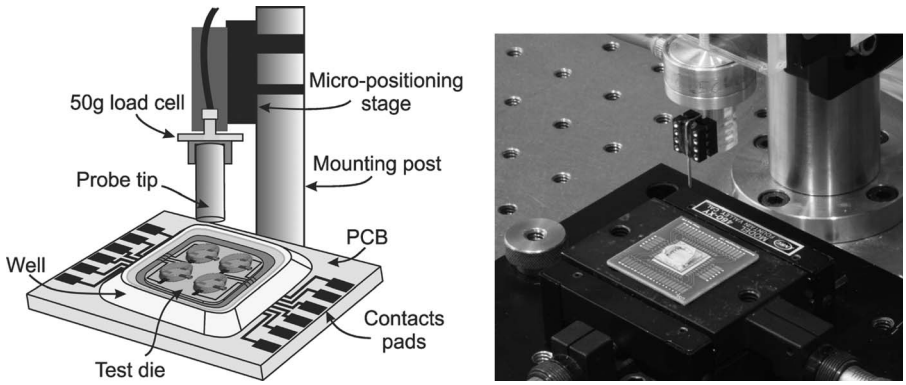

Fig. 5. Experimental setup. A load cell with attached probe tip was mounted to a motorized micropositioning stage with sub micrometer Z-axis positioning capability. Deflection experiments were performed with sensors completely submerged.

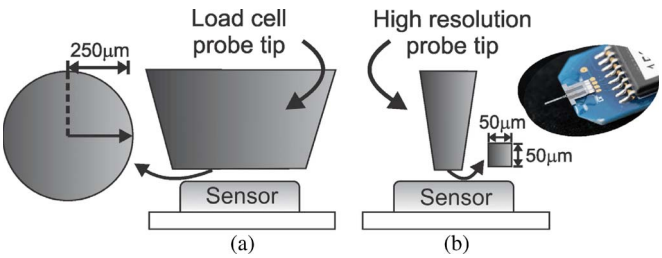

Fig. 6. (a) Flat polished probe tip mounted to load cell used for uniform deflection across entire sensor footprint. (b) High resolution force probe (3 mm long, 50×50 μm) with microNewton resolution (Femtotools). Smaller probe provides high resolution force measurements not possible with the standard load cell and approximates deflection characteristics under a central point force.

user-defined deflection profiles. For high resolution force measurements, a silicon force probe (50×50 μm tip) with microNewton force resolution was utilized (ST-150, Femtotools HmGb, Zurich, Switzerland). The smaller probe head allowed for precise force measurements applied centrally on the sensor surface Fig. 6(b). Assuming that a centrally applied point force F can be translated to an evenly distributed pressure P over a membrane of radius r through the relation $F = P\pi r^2$, it can be shown that a centrally point-force-loaded diaphragm will deflect four times that of uniformly loaded diaphragm [40]. This relation provides a useful and approximate basis for comparison between high resolution measurements and those performed with the load cell. High resolution force measurements were attained up to a maximum of 3000 μN (the probe overload limit).

V. Results and Discussion

The typical deflection profile consisted of a constant velocity (2 μm/s) downward deflection followed by release, with a dwell time of approximately 3 s at the maximum deflection. This profile was repeated twice for each depth between 6 and 18 μm in increments of 2 μm [Fig. 7(a)]. During sensor deflection, temporal responses of both force and impedance were recorded at a sampling rate of 4 Hz. Over a period of several minutes, these responses were robust and repeatable with deflection steps clearly discernable through elevated impedance and force measurements [Fig. 7(b)].

A. Finite-Element Modeling

A nonlinear finite-element model (FEM) of the Parylene microchamber was developed and tested to model its force–deflection performance (COSMOSWorks 2009, Dassault Systèmes SolidWorks Corporation, Concord, MA). A nonlinear model provided greater accuracy in capturing sensor dynamics outside of the small deflection range. Typical values reported in the literature for thin-film Parylene were utilized for this model [43]. Forces in the range of 10 mN (applied normally over the full sensor contact surface) indicated deflections of 10–12 μm or approximately 50% of device span and agree quite well with experimental results (Fig. 8). Compared to the analytical solution for circular diaphragms, the FEM simulation produced larger deflections for a given force which is reasonable given the fixed, rigidly clamped boundary conditions assumed by the analytical solution.

Experimental data was attained using a load cell which provided a large force measurement range but low precision particularly at small loads which may account for some of the discrepancy between the experimental data and the FEM particularly in the range below 5 mN. Another source may arise from the model assumption of a strictly normal application of force on the diaphragm throughout the deflection range. This is somewhat different experimentally as slight deviations from normal are expected as diaphragm curvature is introduced. Yet, another possible source is the introduction of a slight convexity to the diaphragm which is not captured in the FEM model. It is reasonable to expect some slight deviation from an ideally flat diaphragm when utilizing very thin flexible films filled with solution. At low convexity ratios, in the region of small deflection (< 2 μm), the response is characterized by a very close (or slightly lower) deflection than predicted followed by a region of greater deflection than predicted by the models [40]. The net result would be a noticeably steeper gradient than predicted in the region below 5 mN. The response curve at large deflection would remain largely unaffected. Nevertheless, these models are useful in providing an estimate of the range of loads expected over the full range of sensor deflection. Although the simulations and analytical models do not capture any coupling between the fluid and sensor microstructures, the measured responses still agree

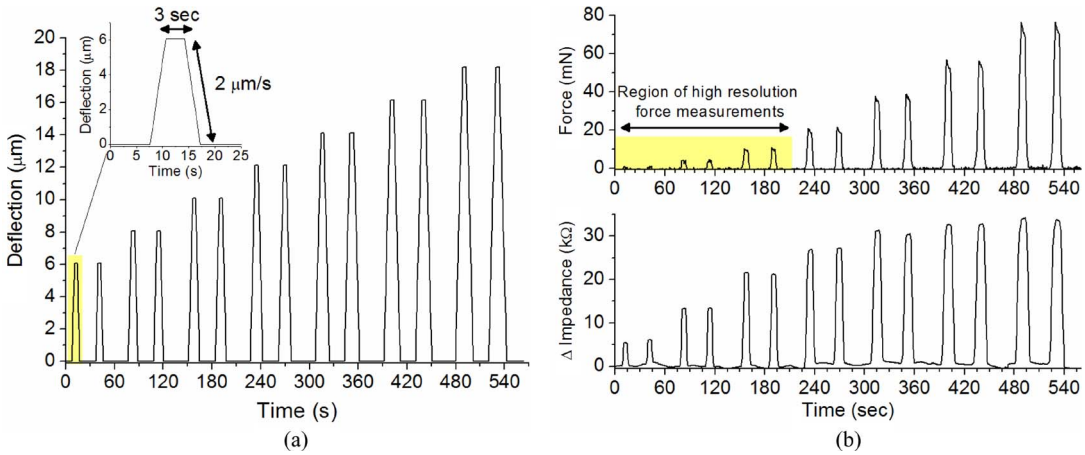

Fig. 7. (a) Typical deflection profile. Deflections were performed twice at each depth and incremented by 2 μm after each cycle. (b) Typical force and impedance response measured concurrently during deflections cycles. Load cell force response is shown with typical region of interest for high resolution measurements indicated.

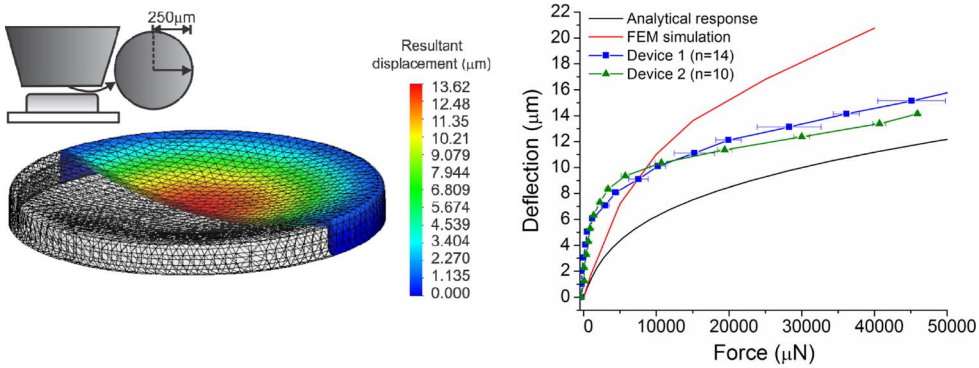

Fig. 8. Nonlinear finite-element simulation of the force–deflection loading response. Comparison of theoretical, simulated and measured force–deflection responses (mean $\pm$ SE, $n \geq 10$).

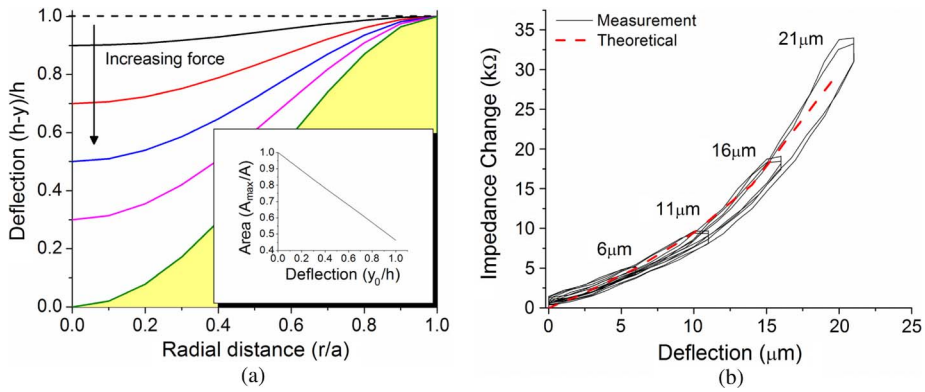

Fig. 9. (a) Normalized deflection as a function of radial distance from the center of the sensor. Shaded area indicates cross-sectional area calculated for one deflection curve (membrane touch-down). The dependence of normalized cross-sectional area with maximum center deflection is shown in the inset. (b) Theoretical curve and representative data demonstrating the relationship between impedance and deflection.

quite well with both simulated and analytical solutions. This suggests that for the aqueous electrolytes, surface tension and viscosity have a minimal effect on the mechanical performance of the sensor under static conditions. At higher loading frequencies, these factors will likely play a larger role in the sensor dynamics but their effects under these conditions were not investigated here.

B. Force Response

The ability to accurately track deflections using EI ultimately determines the resolution and sensitivity of this approach. Membrane deflection as function of radial distance r is shown in Fig. 9(a) for several levels of increasing force. The dependence of cross-sectional area on central membrane deflection (y_0, $r/a = 0$,) is highlighted in the inset. With all other

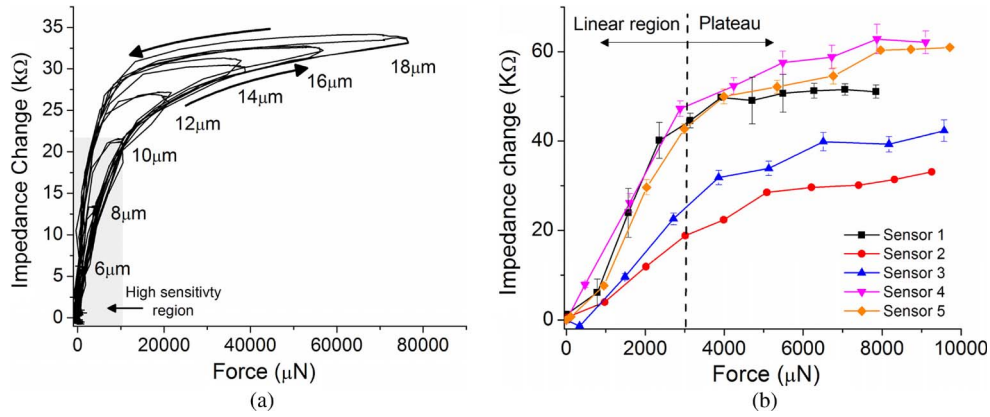

Fig. 10. Impedance–force responses as measured with load cell and large probe tip. (a) Impedance–force curves of a single sensor. Two deflection cycles are performed at each deflection depth. (b) Average responses of five unique devices in 0–10 mN force range. Averaged points were interpolated from data. Error bars include loading/unloading hysteresis (mean ± SE, $n \geq 8$).

parameters constant, the cross-sectional area is directly proportional to deflection, $(A \propto ky_0)$ where k is a negative constant that depends on a and h. The impedance however, is an inverse function of the cross-sectional area between the electrodes, as per (2), $(|Z| \propto 1/A)$, and therefore also varies inversely with sensor deflection $(|Z| \propto 1/y_0)$. The impedance response is therefore expected to vary nonlinearly in similar fashion to capacitance-based sensors that utilize electrode separation as the measurement variable. EI-based tracking of deflection proved to be robust and repeatable Fig. 9(b). Without utilizing any additional signal conditioning techniques, it was possible to resolve membrane deflections at submicron levels (typically 250 nm) yielding a calculated minimum force resolution of ± 22.5 μN. Although this relationship is inherently nonlinear, it is clear that impedance provides an accurate and reliable method for tracking sensor deflection.

Plotting real-time impedance–force data generates characteristic response curves capturing sensor behavior during loading/unloading cycles. The data were repeatable and robust with maximum forces measured up to 79 mN at full sensor deflection. Impedance–force curves at various levels of deflection for a single sensor are provided in Fig. 10(a). The impedance–force response was reproducible and repeatable over fourteen deflection cycles. The most sensitive range of measurement was found below 8–10 μm of deflection coinciding favorably with a region of linearity and minimal hysteresis. Beyond this range, impedance–force response demonstrated built-in hysteresis likely due to viscoelastic deformation of the Parylene. FEM modeling of Von Mises stresses at these elevated deflection values indicated stress magnitudes near the yield strength of Parylene (59 MPa) [43] and provided an indication of the practical limits for completely elastic sensor operation. It is worth noting that following an initial rapid increase where response is quite linear, the impedance response plateaus beyond about 10 μm of deflection coinciding with the nonlinear region of the force–deflection curve.

A similar characteristic response was observed across five unique sensors tested with a minimum of eight deflections cycles each [Fig. 10(b)]. Maximum changes in the nominal impedance ranged 35–60 kΩ (measured in the plateau region > 3000 μN) over steady-state impedance values. An average sensitivity of 10.6 ± 3.7 Ω/μN (mean ± SD, $n = 5$) was measured in the linear region of operation (< 3000 μN). A summary of key performance parameters is provided in Table I. Although individual sensor responses were quite consistent, some variation was observed between individual sensors. The average nominal value of the resting impedance was 1.11 MΩ$(n = 5)$ but ranged from 0.5–1.8 MΩ. Variation in the maximum normalized sensor response was also observed and ranged between 4% and 10%. These differences are thought to arise from photoresist residue remaining in the chambers which can impact the conductivity of the medium. The removal process is diffusion limited, and although sufficient time was allotted for near complete removal across a majority of devices, some residue was still visible in a few devices. Further variability may also be introduced during fabrication, specifically in controlling membrane thickness and sensor height from batch to batch.

TABLE I
PERFORMANCE OF FIVE UNIQUE SENSORS WITH DI WATER AS WORKING ELECTROLYTE

Sensor	Nominal Resting Impedance (kΩ)	Maximum Impedance Change (kΩ)	Maximum Sensitivity (Ω/μN)
1	480-510	50	12.6
2	633-642	35	5.54
3	1780	47.5	7.99
4	950	75	14.5
5	1700	61	12.5

C. Diaphragm Convexity

Device performance is a function of several factors including membrane thickness, device diameter, and convexity [40]. The effect of diaphragm convexity was clearly noted by the response of devices that underwent hard-baking following the patterning of the chamber sacrificial layer. It is well known that additional baking results in photoresist reflow and consequently, more rounded features. The additional baking step therefore results in a convex photoresist sacrificial layer for the chamber as verified by surface profilometry. This shape is replicated in the Parylene chamber diaphragm and results in a response with very different

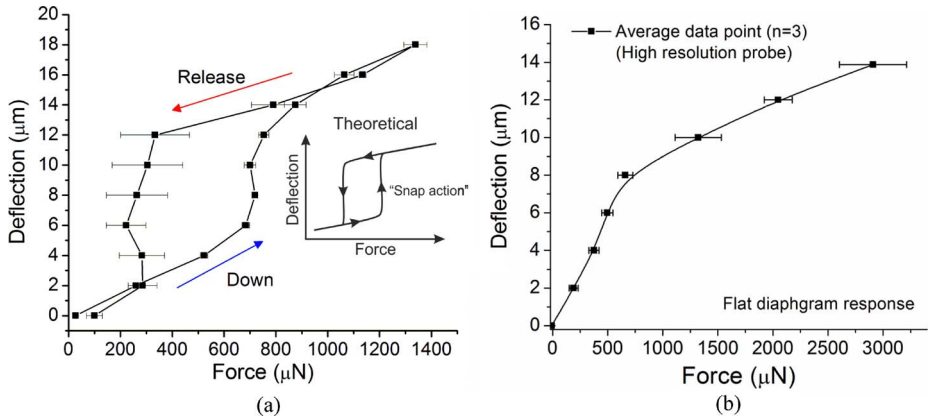

Fig. 11. Force–deflection data attained with high resolution force probe. (a) Convexity was observed following the addition of a baking step during fabrication. Representative data for one loading cycle with a high resolution force probe is shown. Error bars indicate time-averaged force values for each 2 μm deflection step applied (mean $\pm$ SD, n $\leq$ 20). The generalized characteristic response of a convex diaphragm is provided in the inset. (b) Response of flat diaphragm provided for comparison.

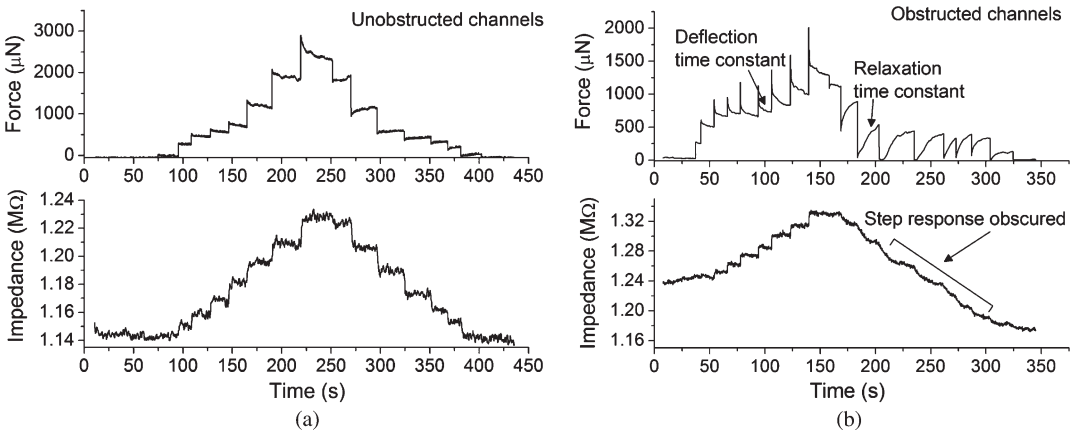

Fig. 12. High resolution force and impedance responses of two individual sensors during a loading/unloading cycle (2 μm step increments). Data were acquired at 4 Hz. (a) Sensor response with unobstructed fluidic access. (b) Sensor response with obstructed fluidic access, provided for comparison.

characteristics. Convex diaphragms exhibit significant hysteresis including a dead-band region over which "snap action" occurs. Snap action is characterized by a sudden step-like increase in deflection at a threshold force level. However, this "snap" point occurs at different points during the loading/unloading cycle resulting in the observed hysteresis. Measurements with the high resolution force probe were particularly useful in capturing the convexity effect which was evident only at low force levels and indicated nearly 5 μm of travel prior to the snap point for the sensor tested [Fig. 11(a)]. It should be noted that the initial distance required to reach the snap point must be accounted for when comparing to the force–deflection curves of a flat diaphragm [Fig. 11(b)]. Due to the smaller probe tip used for these measurements, the magnitude of the forces generated is expected to be approximately 3–4 times smaller than those generated under the large tip condition. This characteristic response was observed over four separate runs on one device. For force sensing applications, this behavior is generally undesirable; however, it may be useful in other applications such as push-buttons and threshold detection. The response can be tailored by controlling the bake time and thus convexity ratio of the diaphragm.

D. Temporal and Frequency Response

The effective spring constant of the diaphragm was estimated from the small deflection response and measured to be approximately 266 N/m. The resonant frequency f_n of the Parylene diaphragm with a clamped edge boundary condition in air was calculated to be $f_n = 811$ Hz as determined by the relation $f_n = 9.22\ \mathrm{t/a}^2[E/\sigma(1-\mu^2)]^{1/2}$ where σ is the density of the diaphragm material [40]. A more accurate value accounts for the viscous damping of the fluid surrounding the diaphragm. Scaling by $(1+\beta)^{-1/2}$, where $\beta = 0.699(\sigma_\mathrm{f} a/\sigma h)$ and σ_f/σ is the density ratio of the fluid to diaphragm material, yields a resonant frequency of 222 Hz. It is expected that further accounting for the hydraulic resistance across the two access ports will reduce this value even further. However, given that there was no observable time constant in the data that were acquired at a rate of 4 Hz [Fig. 12(a)], a conservative estimate would place the nominal value of the resonance frequency on the order of 10–50 Hz, which in most cases is sufficient for tracking forces generated in surgical settings over time scales of minutes to hours. The flow resistance through channels/port structures was not found to be a significant factor to proper device operation under the conditions of interest; clear step-like

responses were observed during both deflection and release. Further characterization would however be necessary to fully assess the frequency response under rapid loading/unloading cycles.

In some cases, however, the force response exhibited a clear time constant during both deflection and release. The value of the time constant was estimated from the data to be 10–12 s [Fig. 12(b)]. This was assessed by applying discrete deflection/release steps in 2 μm increments. The slow-adapting behavior was most notable in the force response; however, it was also observed in the impedance response during the release cycle. The observed behavior was attributed to flow constriction through the fluidic access ports and possible port collapse. It is important that fluid flow into and out of the structure is not impeded so as to not inhibit the mechanical behavior of the chamber. Occlusion or insufficient opening of the fluid access ports during fabrication significantly altered the desired mechanical behavior. Additional channels or larger ports may help in reducing the chance of failure due to blockage as well as reducing the effects of hydraulic resistance.

E. Applications and Additional Considerations

To our knowledge, this is the first demonstration of force measurement utilizing EI as the basis for transduction within a microdevice. This technique was previously demonstrated for robotic tactile sensing applications at larger scales with biomimetic models of the human digit [44] but required advanced signal conditioning to extract force and feature information. Compared to other polymer-based approaches, EI-based transduction provides a new alternative to resistive and capacitive techniques [45], [46]. A significant advantage over conventional elastomeric approaches is the potential for reducing crosstalk between sensor elements. Because the sensors are independent and not embedded within a bulk material, the lateral crosstalk encountered by embedded approaches is significantly reduced. Silicon-based approaches also predominantly use capacitive or piezoresistive transduction and have produced a variety of sensor technologies. Many of these technologies have been introduced for tactile feedback as part of minimally invasive surgery applications with some success [12]; however, packaging and flexibility issues remain. The combination of sensitivity and simple packaging afforded by fluid-filled impedance-based sensors provides an attractive alternative to these technologies.

For neural prosthetic applications involving the implantation of devices into the brain, spinal cord, or retina, very few sensor solutions exist. The integration of sensor technology for such applications could assist in improving implant design, material selection, and the understanding of biomechanical interaction at these interfaces. Many neural prosthetic applications employ small probes [47], flat electrode arrays, or flexible substrates [20], [22] making integration of existing sensor technologies into these systems challenging. The Parylene-based technology presented here addresses the need for biocompatibility, waterproofing, and a packaging approach tailored to the working environment. Force measurement capability below 1 mN is also desirable because the nervous tissues of the body are known to be some of the softest [48], [49] with Young's modulus values typically in the 1–20 kPa range. Impedance-based force sensors offer a unique sensing approach to these operating conditions. A potential limitation to the current approach lies in the Parylene-Parylene interfaces which can be susceptible to delamination if soaked for an extended period of time. Annealing of the Parylene films above the glass transition temperature has proved useful in addressing this issue but was not performed here; however, no such delamination was observed during the course of our experiments. Although Parylene was selected as the structural material in this design, other materials such as silicones or polyimides could potentially be used in conjunction with the impedance-based sensing technique to realize novel sensor designs.

VI. Conclusion

Fluid-filled Parylene-based microstructures were designed, fabricated, and demonstrated for high sensitivity force measurements. A low temperature fabrication process was developed utilizing multilayered Parylene structures and stacked sacrificial photoresist. This technique requires minimal packaging and utilizes the ambient operating solution as the basis for electrochemical measurements. Impedance-based transduction of externally applied forces was shown to be a highly sensitive measurement technique as is compatible with liquid environments. The small form factor, flexible substrate, ease of integration, and highly sensitive response provides a useful combination of features making these sensors attractive for use with biomedical force sensing applications.

Acknowledgment

The authors would like to acknowledge Mr. B. Kim for invaluable assistance with the experimental setup and device characterization. We would also like to thank Dr. D. Zhu and the members of the USC Biomedical Microsystems Laboratory for their assistance.

References

[1] Y. Suzuki and Y.-C. Tai, "Micromachined high-aspect-ratio Parylene beam and its application to low-frequency seismometer," in *Proc. IEEE MEMS*, Kyoto, Japan, 2003, pp. 486–489.

[2] P.-J. Chen, D. C. Rodger, M. S. Humayun, and Y.-C. Tai, "Unpowered spiral-tube Parylene pressure sensor for intraocular pressure sensing," *Sens. Actuators A, Phys.*, vol. 127, no. 2, pp. 276–282, Mar. 2006.

[3] C. A. Gutierrez and E. Meng, "A subnanowatt microbubble pressure sensor based on electrochemical impedance transduction in a flexible all-Parylene package," in *Proc. IEEE MEMS*, Cancun, Mexico, 2011, pp. 549–552.

[4] Z. Fan, J. M. Engel, J. Chen, and C. Liu, "Parylene surface-micromachined membranes for sensor applications," *J. Microelectromech. Syst.*, vol. 13, no. 3, pp. 484–490, Jun. 2004.

[5] P.-Y. Li, R. Sheybani, C. A. Gutierrez, J. T. W. Kuo, and E. Meng, "A Parylene bellows electrochemical actuator," *J. Microelectromech. Syst.*, vol. 19, no. 1, pp. 215–228, Feb. 2010.

[6] T. N. Pornsin-Sirirak, Y. C. Tai, H. Nassef, and C. M. Ho, "Flexible Parylene actuator for micro adaptive flow control," in *Proc. IEEE MEMS*, Interlaken, Switzerland, 2001, pp. 511–514.

[7] H.-S. Noh, Y. Huang, and P. J. Hesketh, "Parylene micromolding, a rapid and low-cost fabrication method for Parylene microchannel," *Sens. Actuators B, Chem.*, vol. 102, no. 1, pp. 78–85, Sep. 2004.

[8] X.-Q. Wang, Q. Lin, and Y.-C. Tai, "A Parylene micro check valve," in *Proc. IEEE MEMS*, Orlando, FL, 1999, pp. 177–182.

[9] P.-J. Chen, D. C. Rodger, E. M. Meng, M. S. Humayun, and Y.-C. Tai, "Surface-micromachined Parylene dual valves for on-chip unpowered microflow regulation," *J. Microelectromech. Syst.*, vol. 16, no. 2, pp. 223–231, Apr. 2007.
[10] C. A. Gutierrez and E. Meng, "Improved self-sealing liquid encapsulation in Parylene structures by integrated stackable annular-plate stiction valve," in *Proc. IEEE MEMS*, Hong Kong, 2010, pp. 524–527.
[11] S. Yang and T. Saif, "Micromachined force sensors for the study of cell mechanics," *Rev. Sci. Instrum.*, vol. 76, no. 4, pp. 044 301-1–044 301-8, Apr. 2005.
[12] M. E. H. Eltaib and J. R. Hewit, "Tactile sensing technology for minimal access surgery—A review," *Mechatronics*, vol. 13, no. 10, pp. 1163–1177, Dec. 2003.
[13] J. Tegin and J. Wikander, "Tactile sensing in intelligent robotic manipulation—A review," *Ind. Robot, Int. J.*, vol. 32, no. 1, pp. 64–70, 2005.
[14] A. Menciassi, A. Eisinberg, M. C. Carrozza, and P. Dario, "Force sensing microinstrument for measuring tissue properties and pulse in microsurgery," *IEEE/ASME Trans. Mechatronics*, vol. 8, no. 1, pp. 10–17, Mar. 2003.
[15] K. Noda, K. Hoshino, K. Matsumoto, and I. Shimoyama, "A shear stress sensor for tactile sensing with the piezoresistive cantilever standing in elastic material," *Sens. Actuators A, Phys.*, vol. 127, no. 2, pp. 295–301, Mar. 2006.
[16] L. Han, J. A. Noble, and M. Burcher, "A novel ultrasound indentation system for measuring biomechanical properties of in vivo soft tissue," *Ultrasound Med. Biol.*, vol. 29, no. 6, pp. 813–823, Jun. 2003.
[17] D. B. Plewes, J. Bishop, A. Samani, and J. Sciarretta, "Visualization and quantification of breast cancer biomechanical properties with magnetic resonance elastography," *Phys. Med. Biol.*, vol. 45, no. 6, pp. 1591–1610, Jun. 2000.
[18] A. Samani, J. Bishop, C. Luginbuhl, and D. B. Plewes, "Measuring the elastic modulus of ex vivo small tissue samples," *Phys. Med. Biol.*, vol. 48, no. 14, pp. 2183–2198, Jul. 2003.
[19] M. Tokida, T. Obara, M. Takahashi, M. Yamato, and S. Konishi, "Integration of cell sheet sucking and tactile sensing functions to retinal pigment epithelium transplantation tool," in *Proc. IEEE MEMS*, Hong Kong, 2010, pp. 316–319.
[20] D. C. Rodger, A. J. Fong, W. Li, H. Ameri, A. K. Ahuja, C. A. Gutierrez, I. Lavrov, H. Zhong, P. R. Menon, E. Meng, J. W. Burdick, R. R. Roy, V. R. Edgerton, J. D. Weiland, M. S. Humayun, and Y.-C. Tai, "Flexible Parylene-based multielectrode array technology for high-density neural stimulation and recording," *Sens. Actuators B, Chem.*, vol. 132, no. 2, pp. 449–460, Jun. 2008.
[21] D. C. Rodger, W. Li, H. Ameri, A. Ray, J. D. Weiland, M. S. Humayun, and Y.-C. Tai, "Flexible Parylene-based microelectrode technology for intraocular retinal prostheses," in *Proc. IEEE Nano/Micro Eng. Mol. Syst.*, 2006, pp. 743–746.
[22] J. D. Weiland, W. Liu, and M. S. Humayun, "Retinal prosthesis," *Annu. Rev. Biomed. Eng.*, vol. 7, pp. 361–401, 2005.
[23] J. Rosenhorn and N. H. Diemer, "Reduction of regional cerebral blood flow during brain retraction pressure in rat," *J. Neurosurg.*, vol. 56, no. 6, pp. 826–829, Jun. 1982.
[24] T. W. Berger and D. L. Glanzman, *Toward Replacement Parts for the Brain*. Cambridge, MA: MIT Press, 2005.
[25] J. Dargahi, S. Najarian, and B. Liu, "Sensitivity analysis of a novel tactile probe for measurement of tissue softness with applications in biomedical robotics," *J. Mater. Process. Technol.*, vol. 183, no. 2/3, pp. 176–182, Mar. 2007.
[26] H. Roham, S. Najarian, S. M. Hosseini, and J. Dargahi, "Design and fabrication of a new tactile probe for measuring the modulus of elasticity of soft tissues," *Sens. Rev.*, vol. 27, no. 4, pp. 317–323, 2007.
[27] G. Vásárhelyi, M. Ádám, É. Vázsonyi, I. Bársony, and C. Dücso, "Effects of the elastic cover on tactile sensor arrays," *Sens. Actuators A, Phys.*, vol. 132, no. 1, pp. 245–251, Nov. 2006.
[28] C. A. Gutierrez and E. Meng, "Parylene-based electrochemical-MEMS transducers," *J. Microelectromech. Syst.*, vol. 19, no. 6, pp. 1352–1361, Dec. 2010.
[29] C. A. Gutierrez and E. Meng, "A dual function Parylene-based biomimetic tactile sensor and actuator for next generation mechanically responsive microelectrode arrays," in *Proc. IEEE TRANSDUCERS, Solid-State Sens., Actuators, Microsyst. Conf.*, Denver, CO, 2009, pp. 2194–2197.
[30] M. E. Orazem and B. Tribollet, *Electrochemical Impedance Spectroscopy*. Hoboken, NJ: Wiley, 2008.
[31] M. A. Schwarz and P. C. Hauser, "Recent developments in detection methods for microfabricated analytical devices," *Lab Chip*, vol. 1, pp. 1–6, 2001.
[32] J. E. B. Randles, "Kinetics of rapid electrode reactions," *Discuss. Faraday Soc.*, vol. 1, pp. 11–19, 1947.
[33] D. Erickson and D. Li, "Integrated microfluidic devices," *Anal. Chim. Acta*, vol. 507, pp. 11–26, 2004.
[34] A. J. Bard and L. R. Faulkner, *Electrochemical Methods: Fundamentals and Applications,* 2nd ed. Hoboken, NJ: Wiley, 2001.
[35] D. A. Robinson, "The electrical properties of metal microelectrodes," *Proc. IEEE*, vol. 56, no. 6, pp. 1065–1071, Jun. 1968.
[36] R. C. Gesteland, B. Howlandt, J. Y. Lettvin, and W. H. Pitts, "Comments on microelectrodes," *Proc. IRE*, vol. 47, no. 11, pp. 1856–1862, Nov. 1959.
[37] C. de Haro, R. Mas, G. Abadal, J. Munoz, F. Perez-Murano, and C. Dominguez, "Electrochemical platinum coatings for improving performance of implantable microelectrode arrays," *Biomaterials*, vol. 23, no. 23, pp. 4515–4521, Dec. 2002.
[38] J. J. Whalen, J. D. Weiland, and P. C. Searson, "Electrochemical deposition of platinum from aqueous ammonium hexachloroplatinate solution," *J. Electrochem. Soc.*, vol. 152, no. 11, pp. C738–C743, 2005.
[39] B. Bhushan, *Handbook of Micro/Nanotribology,* 2nd ed. Boca Raton, FL: CRC Press, 1999.
[40] M. D. Giovanni, *Flat and Corrugated Diaphragm Design Handbook*, vol. 11. New York: Marcel Dekker, 1982.
[41] C. A. Gutierrez, C. McCarty, B. Kim, M. Pahwa, and E. Meng, "An implantable all-Parylene liquid-impedance based MEMS force sensor," in *Proc. IEEE MEMS*, Hong Kong, 2010, pp. 600–603.
[42] R. Bashir, "BioMEMS: State-of-the-art in detection, opportunities and prospects," *Adv. Drug Deliv. Rev.*, vol. 56, no. 11, pp. 1565–1586, Sep. 2004.
[43] C. Y. Shih, T. A. Harder, and Y. C. Tai, "Yield strength of thin-film Parylene-C," *Microsyst. Technol.*, vol. 10, no. 5, pp. 407–411, Aug. 2004.
[44] N. Wettels, V. J. Santos, R. S. Johansson, and G. E. Loeb, "Biomimetic tactile sensor array," *Adv. Robot.*, vol. 22, no. 8, pp. 829–849, 2008.
[45] E.-S. Hwang, J.-H. Seo, and Y.-J. Kim, "A polymer-based flexible tactile sensor for both normal and shear load detections and its application for robotics," *J. Microelectromech. Syst.*, vol. 16, no. 3, pp. 556–563, Jun. 2007.
[46] L. Beccai, S. Roccella, A. Arena, F. Valvo, P. Valdastri, A. Menciassi, M. C. Carrozza, and P. Dario, "Design and fabrication of a hybrid silicon three-axial force sensor for biomechanical applications," *Sens. Actuators A, Phys.*, vol. 120, no. 2, pp. 370–382, May 2005.
[47] K. A. Moxon, S. C. Leiser, G. A. Gerhardt, K. A. Barbee, and J. K. Chapin, "Ceramic-based multisite electrode arrays for chronic single-neuron recording," *IEEE Trans. Biomed. Eng.*, vol. 51, no. 4, pp. 647–656, Apr. 2004.
[48] L. Galli-Resta, P. Leone, D. Bottari, M. Ensini, E. Rigosi, and E. Novelli, "The genesis of retinal architecture: An emerging role for mechanical interactions?" *Prog. Retinal Eye Res.*, vol. 27, no. 3, pp. 260–283, May 2008.
[49] Y.-B. Lu, K. Franze, G. Seifert, C. Steinha, F. Kirchhoff, H. Wolburg, J. Guck, P. Janmey, E.-Q. Wei, J. Kas, and A. Reichenbach, "Viscoelastic properties of individual glial cells and neurons in the CNS," *PNAS*, vol. 103, no. 47, pp. 17 759–17 764, Nov. 2006.

Christian A. Gutierrez (M'09) received B.S. degrees in electrical engineering and business economics and management and the M.S. degree in electrical engineering from the California Institute of Technology (Caltech), Pasadena, in 2005 and 2006, respectively. He is currently working toward the Ph.D. degree in biomedical engineering (under fellowship) at the University of Southern California (USC), Los Angeles.

He currently works at the National Science Foundation's Biomimetic Microelectronic Systems Engineering Research Center, where he is a Co-President of the Student Leadership Council. His past research was carried out in the Caltech Micromaching Laboratory and was focused on identifying, analyzing, and implementing power harvesting and storage circuitry for microelectromechanical-systems-based power harvesting devices. He is currently conducting research toward the development of novel micro- and nanotechnologies for biomedical applications. His specific research is focused on the development of retinal prosthesis technologies to restore sight to the blind.

Mr. Gutierrez was a recipient of the Caltech Presidential Scholarship, Bill and Melinda Gates Millennium Fellowship, and the USC Viterbi School of Engineering Kunzel Fellowship.

Ellis Meng (M'02–SM'09) received the B.S. degree in engineering and applied science and the M.S. and Ph.D. degrees in electrical engineering from the California Institute of Technology (Caltech), Pasadena, in 1997, 1998, and 2003, respectively.

She is an Associate Professor in the Department of Biomedical Engineering, University of Southern California, Los Angeles, where she has been since 2004. She currently holds a joint appointment in the Ming Hsieh Department of Electrical Engineering. Her research interests include bioMEMS, implantable biomedical microdevices, microfluidics, multimodality integrated microsystems, and packaging. She held the Viterbi Early Career Chair in the Viterbi School of Engineering.

Dr. Meng is a member of Tau Beta Pi, the Biomedical Engineering Society, the Society of Women Engineers, and the American Society for Engineering Education. She was a recipient of the Intel Women in Science and Engineering Scholarship, the Caltech Alumni Association Donald S. Clark Award, and the Caltech Special Institute Fellowship. She has also received the NSF CAREER and Wallace H. Coulter Foundation Early Career Translational Research Awards. In 2009, she was recognized as one of the TR35 *Technology Review* Young Innovators under 35.